49th AIAA Aerospace Sciences Meeting including the New Horizons Forum and Aerospace Exposition
4 - 7 January 2011, Orlando, Florida

AIAA 2011-372

# Pressure Fluctuations Beneath Turbulent Spots and Instability Wave Packets in a Hypersonic Boundary Layer

Katya M. Casper*
*School of Aeronautics and Astronautics, Purdue University, West Lafayette, IN 47907-1282*
*Sandia National Laboratories, Albuquerque, NM 87185*

Steven J. Beresh†
*Sandia National Laboratories, Albuquerque, NM 87185*

Steven P. Schneider‡
*School of Aeronautics and Astronautics, Purdue University, West Lafayette, IN 47907-1282*

**The development of turbulent spots in a hypersonic boundary layer was studied on the nozzle wall of the Boeing/AFOSR Mach-6 Quiet Tunnel. Under quiet flow conditions, the nozzle wall boundary layer remains laminar and grows very thick over the long nozzle length. This allows the development of large turbulent spots that can be readily measured with pressure transducers. Measurements of naturally occurring wave packets and developing turbulent spots were made. The peak frequencies of these natural wave packets were in agreement with second-mode computations. For a controlled study, the breakdown of disturbances created by spark and glow perturbations were studied at similar freestream conditions. The spark perturbations were the most effective at creating large wave packets that broke down into turbulent spots. The flow disturbances created by the controlled perturbations were analyzed to obtain amplitude criteria for nonlinearity and breakdown as well as the convection velocities of the turbulent spots. Disturbances first grew into linear instability waves and then quickly became nonlinear. Throughout the nonlinear growth of the wave packets, large harmonics are visible in the power spectra. As breakdown begins, the peak amplitudes of the instability waves and harmonics decrease into the rising broadband frequencies. Instability waves are still visible on either side of the growing turbulent spots during this breakdown process.**

## Nomenclature

| | | | |
|---|---|---|---|
| $\Phi$ | power spectral density $((p/p_\infty)^2/Hz)$ | $Re$ | freestream unit Reynolds number (1/m) |
| $\sigma_{p'}$ | pressure fluctuation intensity (Pa) | $T_0$ | tunnel stagnation temperature (K) |
| $\sigma_{p'-\overline{p}'}$ | intensity of pressure fluctuations minus ensemble average (Pa) | $U_\infty$ | freestream velocity (m/s) |
| | | $U_{le}$ | leading edge convection velocity (m/s) |
| $f$ | frequency (kHz) | $U_{te}$ | trailing edge convection velocity (m/s) |
| $M$ | freestream Mach number | $z$ | tunnel axial coordinate measured from throat (m) |
| $p$ | pressure fluctuation (Pa) | | |
| $p_\infty$ | freestream static pressure (Pa) | | |
| $P_0$ | tunnel stagnation pressure (kPa) | | |

*Research Assistant and Sandia Graduate Intern, Student Member AIAA, kcasper@purdue.edu, (765) 494-3348
†Principal Member of the Technical Staff, Engineering Sciences Center, Associate Fellow AIAA
‡Professor, Associate Fellow AIAA

Sandia is a multiprogram laboratory operated by Sandia Corporation, a Lockheed Martin Company, for the United States Department of Energy's National Nuclear Security Administration under contract DE-AC04-94AL85000.

# I. Introduction

Hypersonic reentry vehicles are subjected to high levels of fluctuating pressures. These intense fluctuations can cause vibration of internal components and lead to structural fatigue. There is a need to predict the magnitude, location, and spatial extent of the pressure fluctuations to better design reentry vehicles. Current designs often use overly conservative estimates of the fluctuations that can lead to heavier vehicles and degraded flight performance. Some correlations exist for the magnitude of transitional and turbulent pressure fluctuations, but these were derived primarily using either incompressible data or conventional (noisy flow) hypersonic wind-tunnel tests.[1–6] Too little physical understanding of the generation of transitional pressure fluctuations has resulted from such modeling efforts.

Wind-tunnel tests at fixed freestream conditions have shown that transitional pressure fluctuations can be more severe than turbulent pressure fluctuations,[3,7–10] making transitional fluctuations of primary interest for this work. The transition process can be described through intermittency and the growth and propagation of turbulent spots in the transitional boundary layer.[11–13] These turbulent spots create wall pressure fluctuations. Recent DNS efforts have computed the pressure field for wave packets and developing turbulent spots in hypersonic boundary layers.[14–16] The resulting wall fluctuations should be identifiable in surface-mounted pressure transducers, though to the authors' knowledge, no measurements of the internal structure of spots in pressure data under a hypersonic boundary layer have been made. By combining the pressure fluctuations associated with a turbulent spot into a model of transition, the spot-based models can be extended to calculate transitional pressure fluctuations.

Previous measurements on a seven-degree half-angle cone showed that the pressure fluctuations peak during transition, but turbulent spots could not be clearly identified in the time traces.[17] This was likely due to the frequency-response limitations of the pressure transducers. The boundary layer on the cone is only a few millimeters thick and transition occurs over a short length. The turbulent spots are small (on the order of a cm) and the sensors used did not have the appropriate frequency response or spatial resolution to detect individual spots. However, the pressure field did show peaks in the skewness and kurtosis of the transitional signal, suggestive of the presence of turbulent spots.[18,19]

In order to study turbulent spots within the instrumentation limits, measurements of turbulent spot pressure fluctuations were made on the nozzle wall of the Boeing/AFOSR Mach-6 Quiet Tunnel (BAM6QT). The BAM6QT can be operated under quiet flow conditions. Under quiet flow, laminar boundary layers are maintained on the wall of the wind tunnel. Laminar flow avoids the generation of pressure-fluctuation "noise" usually radiated from the turbulent walls of conventional tunnels. Because the boundary layer grows over the entire nozzle length, it is at least ten millimeters thick in the test section. As a result, turbulent spots can grow much larger along the nozzle. The smaller spots can be many cm long, with the largest spots on the order of a meter long. These larger spots give better relative resolution with the available pressure sensors, in comparison with the cone measurements.

Naturally occurring wave packets and turbulent spots on the tunnel wall were studied under quiet flow conditions. However, the initial spanwise location of these disturbances relative to the sensors is unknown. In order to study controlled disturbances, two different flow perturbers were used to disturb the flow. A spark perturber was used to create large impulses that would rapidly break down. A glow perturber was also used to generate small wave packets at a given frequency. Linear and nonlinear wave packets as well as their breakdown were measured. By studying controlled disturbances and their breakdown into turbulent spots, a better understanding of the transitional physics can be gained. This increased understanding of the pressure fluctuations associated with transition can be then be included in engineering models for predicting a flight vehicle's environment.

# II. Boeing/AFOSR Mach-6 Quiet Tunnel

The BAM6QT (Figure 1) can be operated as a conventional noisy tunnel or as a quiet tunnel. The tunnel is a Ludwieg tube – a long pressurized tube with a converging-diverging nozzle on the end. The flow passes from the driver tube, through the test section, diffuser, and finally to the vacuum tank. Flow is initiated by bursting a double diaphragm that is located downstream of the diffuser. When the flow begins, an expansion wave travels upstream and then reflects between the upstream end of the driver tube and the contraction. The total pressure and temperature drop with each reflection cycle (every 200 ms) until the tunnel unstarts. Run times of 3–5 s under quiet flow conditions are typical at present. The tunnel uses air as the test gas

and operates with an initial total pressure, $P_0$, of 34–2070 kPa and an initial total temperature, $T_0$, of 430 K. These conditions give a freestream unit Reynolds number range of 0.4–18.3 $\times 10^6/m$, calculated using Keyes' law for viscosity.[20] The current maximum quiet pressure ($P_0$) is 1170 kPa. The test-section diameter is 0.242 m at the nozzle exit, and the nozzle is 2.590 m long. Noise levels vary from 2–4.5% under noisy flow conditions. Under quiet flow conditions, noise levels are approximately 0.05% or less.[21,22]

Obtaining quiet flow in a hypersonic tunnel is not trivial. The nozzle is polished to a mirror finish to avoid roughness-induced transition, and the contraction boundary layer is removed by bleed slots at the throat. A new laminar boundary layer then begins just upstream of the nozzle throat and is maintained through the test section. The air is also filtered to remove particles above 0.01-microns that may damage the nozzle or trip the boundary layer. More details about the BAM6QT development can be found in Ref. 23.

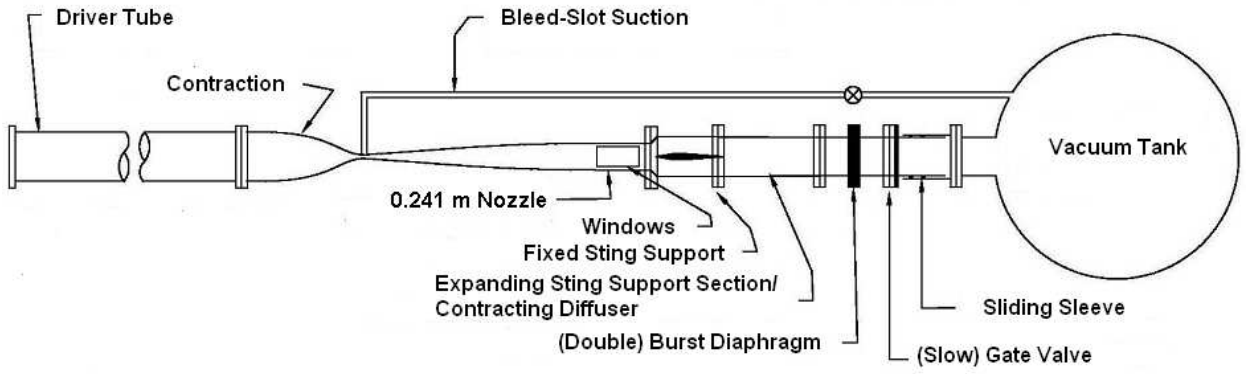


**Figure 1. Boeing/AFOSR Mach-6 Quiet Tunnel**

## III. Experimental Setup

### A. Glow and Spark Perturbers

Two different types of perturbers were used to create disturbances in the boundary layer. A glow perturber was used to introduce perturbations at a specified input frequency. If the input frequency is unstable, the disturbance will grow downstream. The glow perturber electronics used for the study were developed by Ladoon in the 1990's and followed on previous work by other researchers. Details about the glow perturber design and operation are given in Ref. 24. The electrode design developed for the glow-perturber is shown in Figure 2(a). The design consists of a copper inner electrode and an outer brass electrode. High-temperature Macor ceramic is used as an insulator between the electrodes. For these tests, the glow perturber was set to create five cycles of a sine wave at a given frequency between 35 and 60 kHz and pulsed at 200 Hz. By turning the electronics off between bursts, measurements of the resulting disturbances can be made without additional electronic noise from the glow. The amplitude of the waves can be set by controlling the amplitude of the input waveform. For these tests, the input amplitude was set at 8 volts peak to peak. The glow perturber electronics include an amplifier circuit to increase this input by a factor of 10, and a 1:60 step-up transformer further increases the input.

The glow perturber can only create small disturbances at a given frequency. These disturbances require a long region of amplification before breaking down. In order to create larger disturbances that would lead to earlier formation of the turbulent spot, a high-voltage spark perturber was used. The spark perturber creates a rapid, broad frequency impulse instead of generating a discrete frequency sine wave. The spark perturber uses an alternate electrode design to isolate the ground from the tunnel, reducing electrical noise during spark generation (Figure 2(b)). This design has two stainless steel electrodes in a Macor mount. The spark perturber uses an ignition coil and timing circuit to create sparks across the electrode. The ignition coil always remains charged until a spark is desired. When the coil is suddenly shut-off, a spark is created. Similar to the glow perturber, the spark was pulsed at 200 Hz to allow measurements of the resulting disturbances without electrical noise.

(a) (b)

**Figure 2. Electrodes (a) Glow-perturber; (b) Spark-perturber.**

### B. Setup and Instrumentation

Kulite XCQ-062-15A pressure transducers were used to measure pressure fluctuations on the nozzle wall. These transducers use silicon diaphragms as the basic sensing mechanisms. Each diaphragm contains a fully active four-arm Wheatstone bridge. The sensors are mechanically stopped above 103 kPa to prevent damage to the diaphragms at the high BAM6QT pre-run pressures. They have a nominal resonant frequency of 225 kHz. The repeatability of the sensors is approximately 0.1% of the full scale, or 0.1 kPa. The Kulites have screens to protect the diaphragms from damage. For these tests, only A-screen sensors were used. The A-screen has a large central hole. This screen offers only a small amount of diaphragm protection, but the sensor has a flatter frequency response. The sensitive area of the A-screen sensor is the hole size (0.81 $mm^2$).

A schematic of the experimental setup is shown in Figure 3. New hardware had to be constructed to allow pressure measurements on the nozzle wall, just upstream of the nozzle exit. There is a slot in the top wall of the tunnel near the nozzle exit that can be removed to allow traverse measurements with a Pitot probe or a hot wire. A replacement plug was fabricated to fill this slot. It has four mounting holes for Kulite sensors, marked on the axis at the top of Figure 3. Nozzle wall pressure fluctuations were measured with four Kulite XCQ-062-15A pressure transducers in this plug. The Kulites were placed at z = 2.201, 2.302, 2.378, and 2.480 m, where z is the axial tunnel coordinate measured from the throat. The spark and glow perturbers were located at z = 1.924 m, upstream of this plug in another insert on the top wall of the tunnel.

Additional tunnel hardware was constructed to allow measurements downstream of the nozzle exit. Previous measurements have shown that the nozzle wall boundary layer appears laminar well downstream of the nozzle exit.[21,22] In order to take advantage of this additional length of laminar flow, a cylindrical pipe insert was designed that fits between the nozzle exit and the diffuser sting support. This insert has the same diameter of 0.242 m as the nozzle exit. When the tunnel is closed, the pipe insert fits flush with the nozzle exit and extends 0.254 m downstream. Figure 4(a) shows the pipe insert installed in the BAM6QT. At the downstream end of the pipe insert, there is a step at the beginning of a nylon diffuser section (Figure 4(b)). This step was created when the nylon section curled inward during machining. The effect of this step on the present data is discussed in more detail later. A new stainless-steel downstream section is being constructed that will eliminate this step for future tests. For these measurements, Kulites were located at z = 2.628, 2.679, 2.730, 2,781, and 2.831 m on the top wall of the pipe insert. These sensors locations are visible in the photograph in Figure 4(b) and marked on the axis in Figure 3. An additional sensor was placed on the bottom wall of the pipe insert at z = 2.679 m for some runs, to look at the uniformity of quiet flow in the pipe insert.

### C. Data Acquisition

The signal from the Kulite pressure transducers was processed by custom-built electronics, which also supply a 10 V excitation. The output signal was amplified by a gain of 100 with an INA103 instrumentation amplifier chip to give the DC signal. Tektronix TDS7104, TDS5034B, and two DPO7054 Digital Phosphor Oscilloscopes were used for data acquisition. The scopes have an 8-bit vertical resolution, but the resolution can be increased to over 11 bits in Hi-Res mode. Hi-Res mode is used to increase the vertical resolution and provide digital filtering. The oscilloscopes average in real time at the maximum sampling rate and then

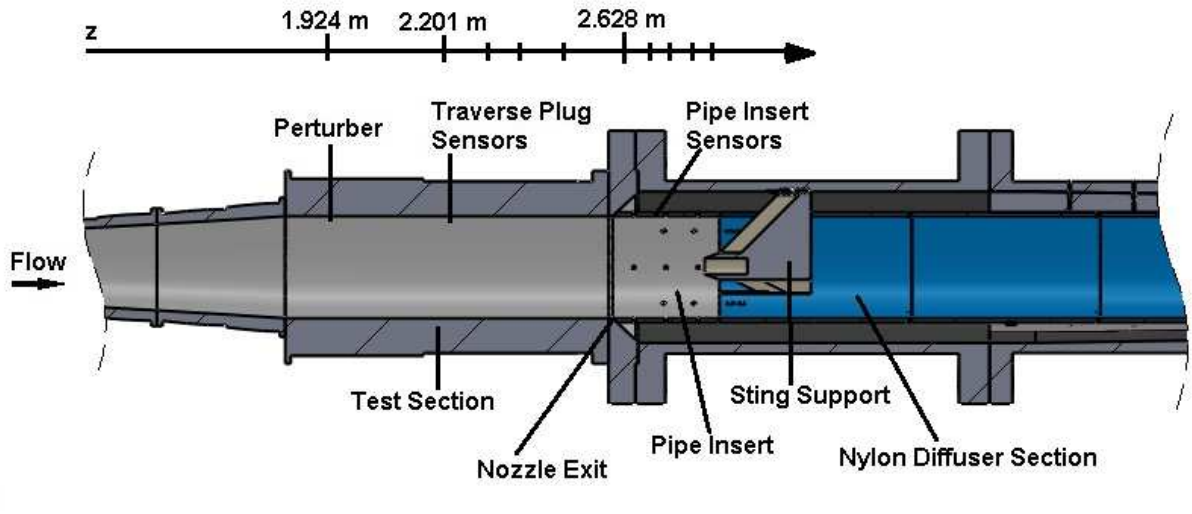


**Figure 3. Schematic of experimental setup in BAM6QT. Perturber and sensor locations are marked on the z axis.**

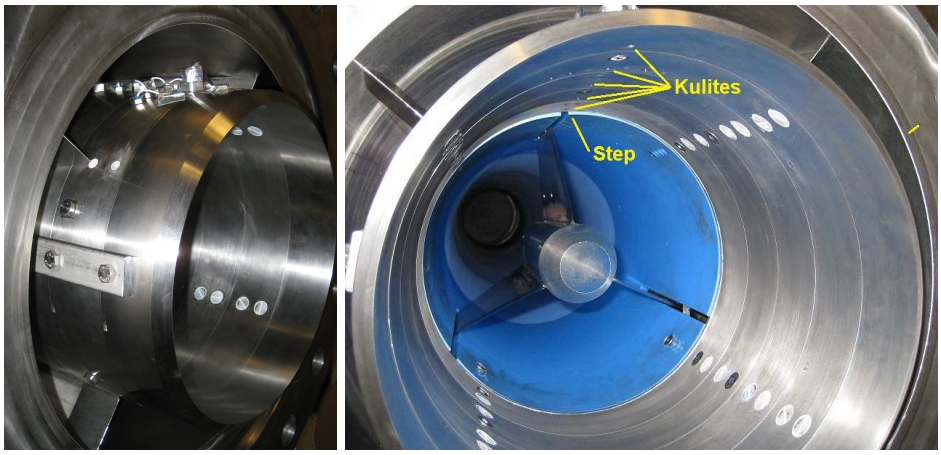


(a) (b)

**Figure 4. Pipe insert installed in the BAM6QT; (a) Looking upstream; (b) Looking downstream.**

save data at the specified sampling rate. The sampling rate for these measurements was 500 kHz. Pressure traces were post-processed by low-pass filtering the data at 150 kHz using a Butterworth filter. This filtering removes sensor resonance from the pressure traces to show the underlying data more clearly.

## IV. Experimental Results

### A. Natural Spot Growth on Nozzle Wall

Under quiet-flow conditions, the nozzle boundary layer is predominantly laminar. These tests showed that this region of laminar flow extends at least 0.254 m past the nozzle exit, throughout the entire pipe insert. These new measurements confirm previous evidence that the boundary layer remains laminar past the nozzle exit.[21,22] However, disturbances sometimes grow and break down intermittently in the boundary layer. As the freestream unit Reynolds number is increased, the disturbances occur more often. Above the maximum quiet freestream unit Reynolds number, transition jumps to somewhere near the tunnel throat, and the boundary layer on the majority of the nozzle wall becomes turbulent. This sudden change probably occurs because some roughness or other disturbance near the throat becomes the dominant transition mechanism

when the boundary layer thins with increasing freestream unit Reynolds number.

Two types of disturbances are typically seen growing in the laminar boundary layer. The first type is a large turbulent spot that develops well upstream in the nozzle. By the time the turbulent spots pass over the sensors that are 2–3 meters downstream, the spots are large and cover most, if not all, of the nozzle circumference. Figure 5 show an example of this large turbulent spot measured in pressure sensors on the top and bottom wall of the BAM6QT. The duration of the spot is similar in both sensors, indicating these large spots span a significant portion of the nozzle circumference. Figure 6 shows typical pressure traces and the associated power spectral densities (PSD's) of these large turbulent spots as they pass over the sensors on the top wall of the tunnel. Each trace is vertically offset from the upstream traces by an amount proportional to its axial tunnel location (z) to make the spot development clear. The sensor closest to the throat is offset the most and the downstream sensors are offset to a lesser degree. Through the middle of the spot, there is a higher mean level than the undisturbed boundary layer. As the spot grows downstream, it elongates, but there is not a large change in the overall pressure fluctuations as indicated by the PSD's. At the last sensor location (z = 2.831 m), a second pressure peak occurs just after the turbulent spot at t = 0.5833 s. It is believed that this is an upstream-traveling reflection of the turbulent spot from the step in the tunnel 0.0254 m downstream of the sensor (Figure 4(b)). This peak occurs only at the downstream end of the pipe insert and has been shown to be sensor independent. A new downstream diffuser section is being constructed to remove this step. It should eliminate this reflection in future tests.

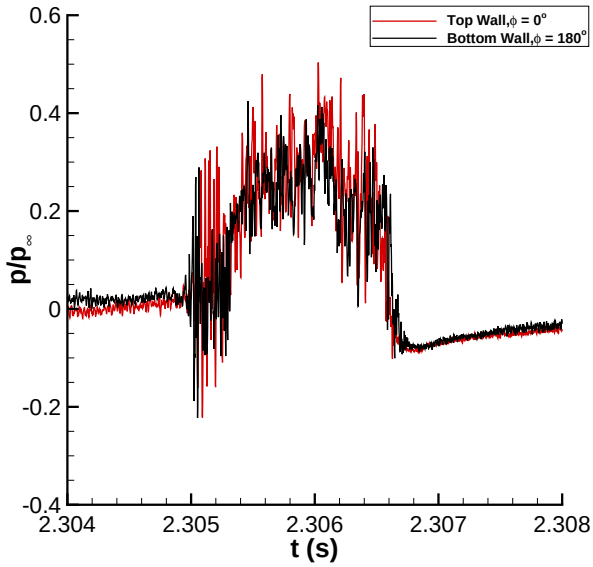


**Figure 5. Large turbulent spot measured on top and bottom wall of BAM6QT, $P_0$ = 1010 kPa, $T_0$ = 414.4 K, $Re = 10.4 \times 10^6/m$.**

The second type of disturbance typically measured is a wave packet that breaks down into a turbulent spot along the nozzle wall. These small disturbances are sporadic during the first two seconds of the run. After two seconds of run time, these disturbances occur much more frequently. Figure 7(a) shows a close-up view of some of these increased fluctuations as they grow downstream. If the traces are contracted to include more time, they resemble turbulent traces. However, expanding the traces shows the flow is punctuated by bursts of wave packets growing into turbulent spots downstream, as seen in Figure 8(a). This noise increase happens on both the top and bottom wall of the tunnel (Figure 7(b)), but the top wall of the tunnel consistently shows much higher disturbance levels than the bottom wall. This noise increase has also been measured by freestream Pitot probes and hot-films mounted on the nozzle wall (pg. 65–72 in Steen[22]).

The reason for this disturbance growth predominantly after t = 2 s and the higher disturbance level on the top wall is unknown. However, measurements made by Borg in 2005 may provide an explanation.[25] His measurements show that there is an increase in total temperature fluctuations in the contraction near this time. Borg attributed this fluctuation increase to the growth of a thick turbulent boundary layer on the upper wall of the contraction. The upper boundary layer grows thicker than the bottom layer and may be due to temperature stratification in the driver tube of the tunnel (the top wall is consistently hotter than

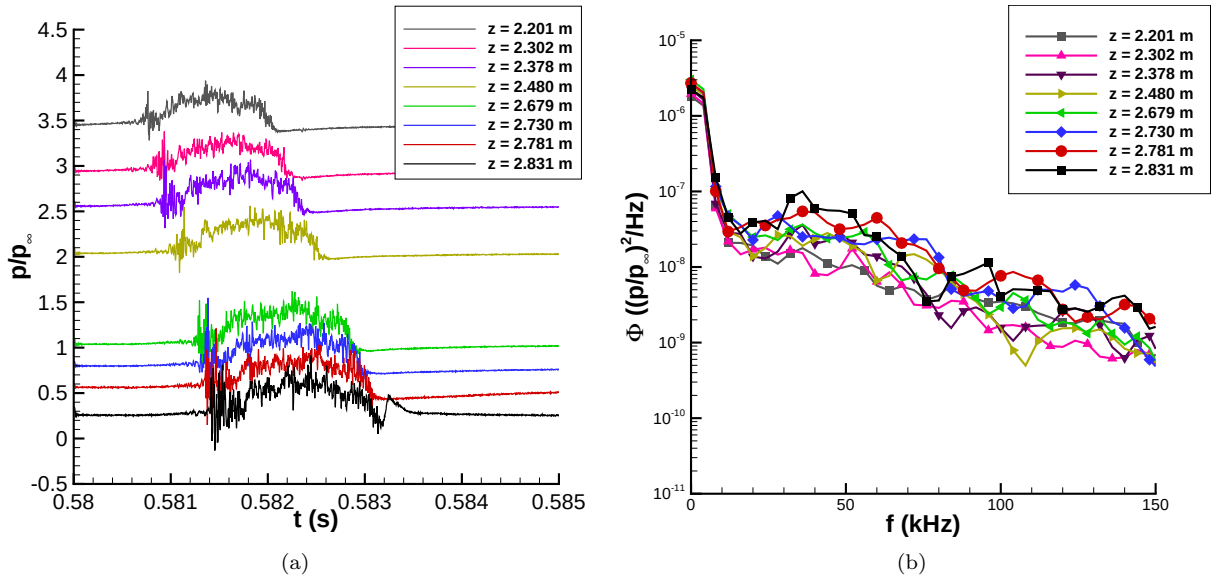


(a) (b)

**Figure 6. Large naturally developed turbulent spot on the nozzle wall, $P_0$ = 1142 kPa, $T_0$ = 428.3 K, $Re = 11.2 \times 10^6/m$; (a) Pressure traces, each trace is vertically offset proportional to z; (b) Power spectral density.**

the bottom wall). Borg's measurements also showed that the fluctuation increase is much larger on the top wall of the tunnel than at the bottom. Even though these measurements point to the origin of the higher pressure fluctuations, more work needs to be done to understand this noise increase.

Figure 8(a) shows close-up pressure traces of an example of the smaller disturbances in the tunnel. Figure 8(b) shows the power spectral density of the pressure traces. In this case, a small wave packet with a peak frequency near 62 kHz can be clearly seen at z = 2.302 m. The wave packet is much larger and becomes nonlinear by z = 2.378 m, as indicated by the presence of a second harmonic. By the following sensor, the packet has begun to break down into a turbulent spot. This breakdown is seen in the PSD as a rise in broadband frequencies. As the spot propagates downstream, it continues to increase in size. Schneider[26] performed instability computations during the design of the BAM6QT nozzle at slightly lower freestream conditions. Those computations indicated the most amplified frequencies of second-mode waves in the nozzle boundary layer at the sensor locations are approximately 50–52 kHz (Figure 33 in Ref. 26). The present measurements are in good agreement with Schneider's computations, as they are taken at slightly higher freestream conditions where the boundary layer would be thinner and lead to higher second-mode wave frequencies. Downstream of the spot, additional second-mode waves appear once the spot grows to a reasonable size. A similar phenomenon has been observed at low speeds where in some conditions Tollmien-Schlichting waves were observed behind turbulent spots.[27]

These results show no evidence of breakdown due to Görtler instabilities; instead, transition downstream on the nozzle wall seems to be dominated by second-mode waves. The long length of the BAM6QT nozzle was designed to reduce the growth of the Görtler instability, and these results suggest that the design was successful in doing so. This second-mode dominated transition seems different from that seen in the former NASA Mach-6 Quiet Tunnel (now in operation at Texas A&M), where Görtler vortices appeared to be the primary transition mechanism.[23]

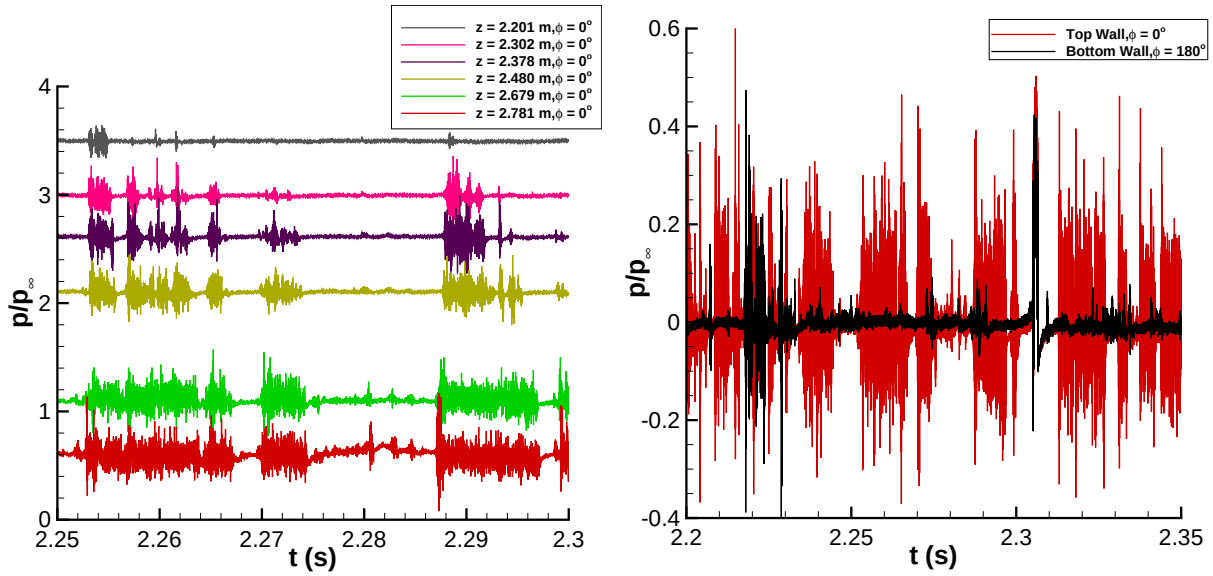


(a) (b)

**Figure 7. Disturbances on nozzle wall, $P_0 = 1010$ kPa, $T_0 = 414.4$ K, $Re = 10.4\times10^6/m$; (a) Pressure disturbances growing downstream, each trace is vertically offset proportional to z; (b) Pressure disturbances on top and bottom walls.**

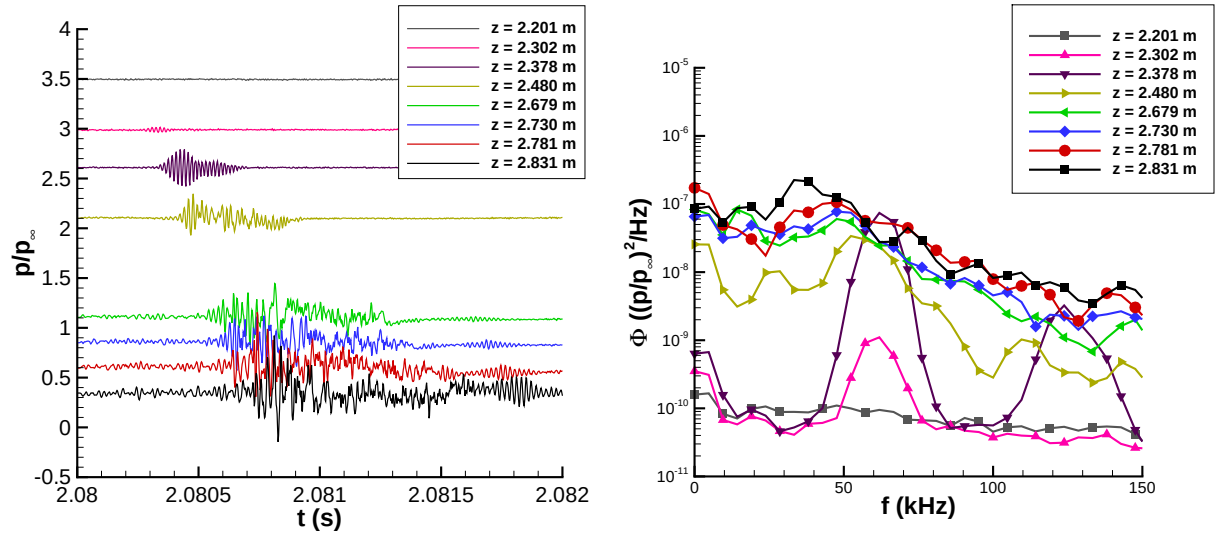


(a) (b)

**Figure 8. Growth of a small turbulent spot on the nozzle wall, $P_0 = 1031$ kPa, $T_0 = 415.9$ K, $Re = 10.6\times10^6/m$; (a) Pressure traces, each trace is vertically offset proportional to z; (b) Power spectral density.**

### B. Growth of Disturbances from Spark Perturbations

The origin of the naturally occurring disturbances on the nozzle wall and their spanwise location relative to the line of sensors is unknown. It is difficult to study the growth and development of these disturbances because they are occurring in an uncontrolled fashion. In order to better study turbulent spot pressure fluctuations, controlled spark perturbations were introduced in the boundary layer at a range of freestream conditions from $Re = 5.76 - 10.8 \times 10^6/m$.

Because the spark perturbations are generated at 200 Hz, multiple disturbances can be averaged. The averaging trigger was the 200-Hz square-wave input signal to the perturber. Ensemble-averaged pressure traces are shown for 50 disturbances. These disturbances were chosen from a 0.5-s interval of a run, after the perturber had been running for a few tenths of a second. More repeatable results are obtained after the perturber has warmed up. Also, even though $Re$ drops within this 0.5-s interval, the change is small and no noticeable affects are seen on the results. Any disturbances that were contaminated by naturally-occurring turbulent spots or smaller disturbances were not used in the averages. An ensemble-averaged power spectral density was also computed by averaging together fast-Fourier transforms (FFT's) from each of the 50 pressure traces and normalizing to obtain the PSD. This ensemble-averaged power-spectral density is not the same as taking a PSD of the ensemble-averaged pressure traces. This difference is most apparent when wave packets began to break down. Even though the packets show good repeatability while growing, their breakdown varies from packet-to-packet, and the pressure fluctuations are no longer in phase. As a result, the ensemble-averaged pressure traces smooth out the turbulent fluctuations seen during breakdown. Since phase information is not contained in the FFT, ensemble averaging FFT's together does not remove the large fluctuations during breakdown but instead creates an average representation of the frequency content of the individual samples.

Figures 9 through 13 show ensemble-averaged waveforms and power spectral densities of the resulting wave packets and their breakdown over the range of tested conditions. At the lowest freestream Reynolds number (Figure 9), a small wave packet develops and grows over the measurement range. The peak frequency decreases from 34 to 19 kHz as the boundary layer thickens downstream. The wave becomes nonlinear and harmonics are visible in the power-spectral densities for z = 2.730 m through z = 2.831 m.

As the Reynolds number continues to increase, the amplitude of the initial disturbance also increases. The waves become nonlinear sooner and then grow much more rapidly. Large nonlinear harmonics are seen in the PSD, in addition to the primary second-mode peak. These harmonics can be very large and in some cases are higher than the broadband frequencies seen after breakdown (Figure 11(b)). Near the last few sensors, the wave packets breakdown into turbulence. This breakdown is clearly seen in the power spectral densities when the peak frequency of the second-mode waves and the harmonics decreases and broadband high frequencies rise towards the peak.

This trend is most clearly seen at the highest $Re$ (Figure 13). The freestream conditions are similar to the naturally occurring disturbances discussed earlier. A wave packet is still initially generated by the spark perturbation. The wave packet grows downstream, and its peak frequency decreases from 50 to 43 kHz. These frequencies are lower than the peak frequency seen in natural disturbance growth at similar conditions and are likely due to the reduced distance, or fetch, for wave growth. The disturbance is introduced well downstream in the nozzle at z = 1.924 m, where the boundary layer is much thicker than near the throat.

Further downstream, the wave packet becomes nonlinear and breaks down into a turbulent spot by z = 2.679 m. Breakdown occurs first in the middle of the packet, with second-mode waves still visible on either side of the breakdown. This shows qualitative agreement with DNS of wave-packet breakdown on a cone in Mach-6 flow where breakdown also began in the middle of a nonlinear wave packet.[16] As the spot grows, the turbulent region lengthens. However, there is still evidence of the second-mode waves on either side of the spot. There is no sudden transition from instability waves to turbulent fluctuations. Instead there is a gradual growth and breakdown of the second-mode waves into turbulent spots. As a result, there is a long region where instability waves are seen while turbulent fluctuations are observed growing within the spot. As the spot grows, the fluctuations at the beginning of the spot are still visible, but the second-mode waves behind the spot become more out of phase and tend to average out in the ensemble average. Again these results show qualitative similarity to DNS. Joksch and Kleiser show the centerline pressure fluctuations in a turbulent spot in a Mach-5 flat-plate boundary layer.[15] Second-mode oscillations are visible at the beginning of the spot and a higher elevated pressure is seen for the remainder of the spot. It is also interesting to note that in Figure 13(a) at z = 2.730 and 2.831 m, a second pressure rise behind the turbulent spots is seen at t = 0.002 and 0.00155 s. As mentioned before for the naturally occurring turbulent spots, this second pressure

rise seems to be a reflection of the turbulent spot from a forward-facing step in the nozzle wall downstream of the spot. The reflection propagates upstream at subsonic speed and rapidly decays.

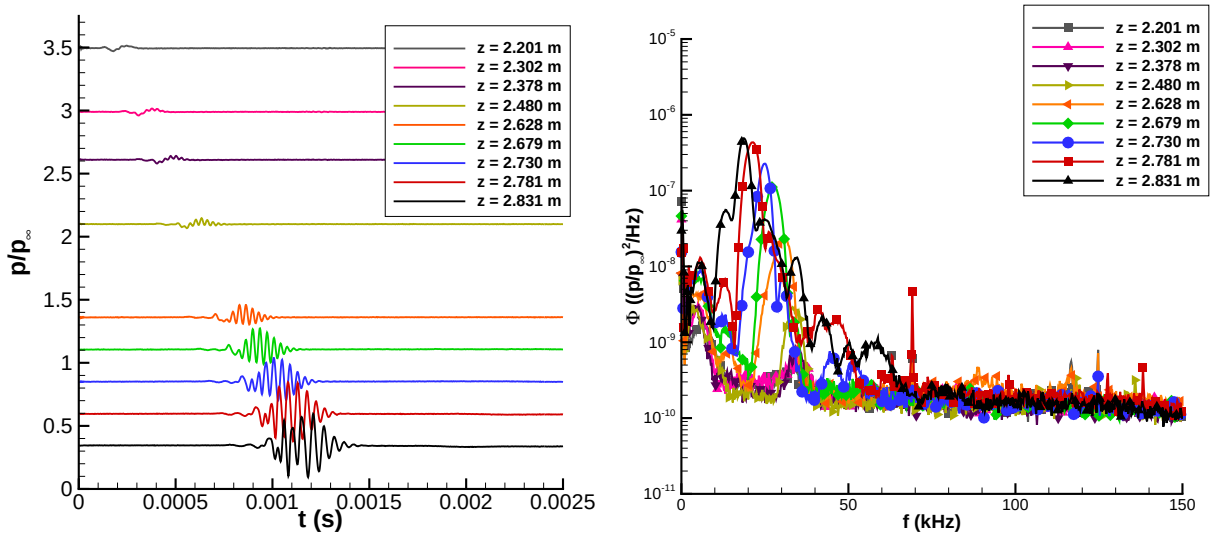


(a) (b)

**Figure 9. Ensemble-averaged disturbances from spark perturbations, $P_0$ = 577.5 kPa, $T_0$ = 424.1 K, $Re = 5.76 \times 10^6/m$; (a) Pressure traces, each trace is vertically offset proportional to z; (b) Power spectral density.**

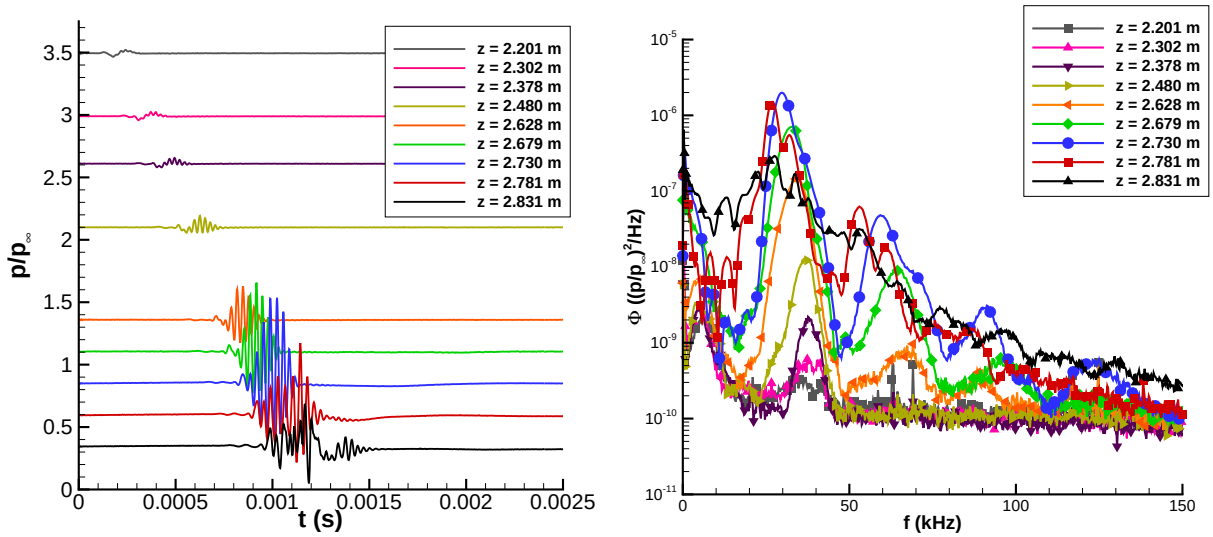


(a) (b)

**Figure 10. Ensemble-averaged disturbances from spark perturbations, $P_0$ = 701.8 kPa, $T_0$ = 423.8 K, $Re = 7.00 \times 10^6/m$; (a) Pressure traces, each trace is vertically offset proportional to z; (b) Power spectral density.**

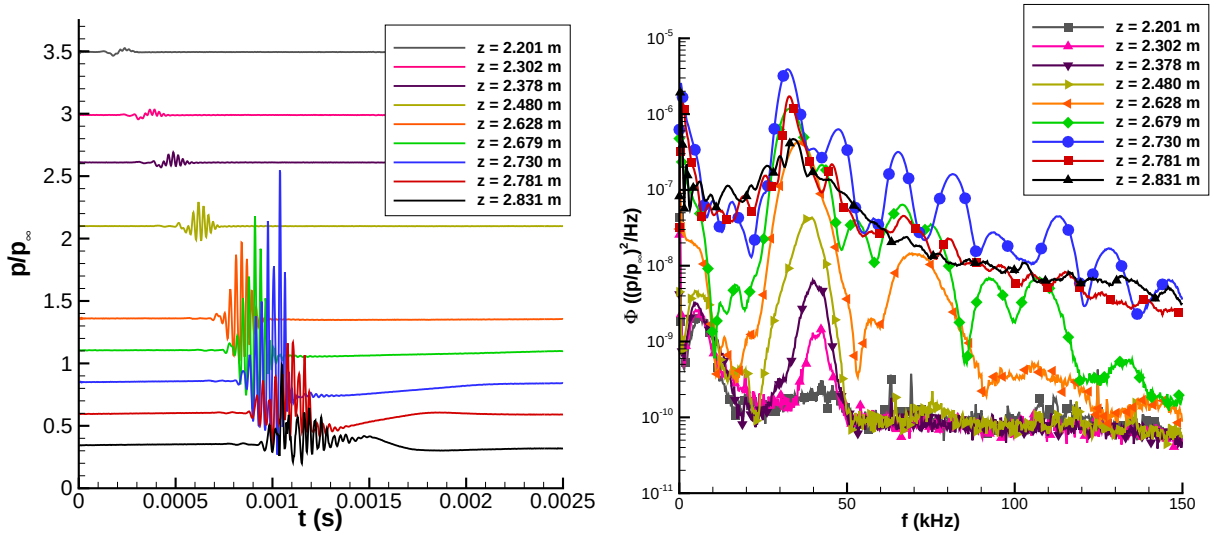


(a) (b)

**Figure 11. Ensemble-averaged disturbances from spark perturbations, $P_0$ = 827.9 kPa, $T_0$ = 424.0 K, $Re = 8.25 \times 10^6/m$; (a) Pressure traces, each trace is vertically offset proportional to z; (b) Power spectral density.**

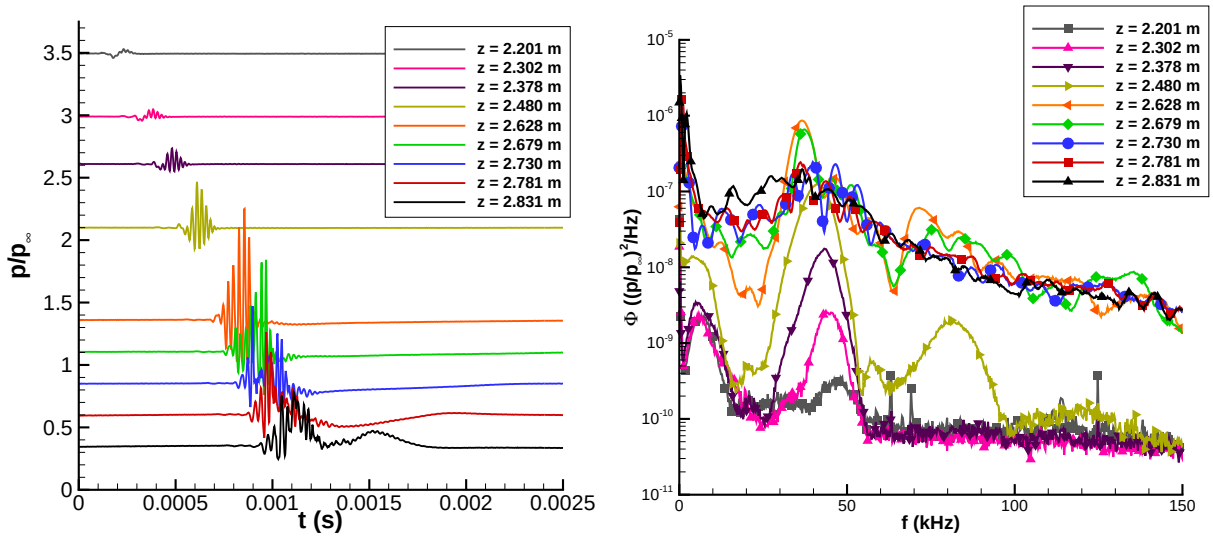


(a) (b)

**Figure 12. Ensemble-averaged disturbances from spark perturbations, $P_0$ = 954.8 kPa, $T_0$ = 423.8 K, $Re = 9.53 \times 10^6/m$; (a) Pressure traces, each trace is vertically offset proportional to z; (b) Power spectral density.**

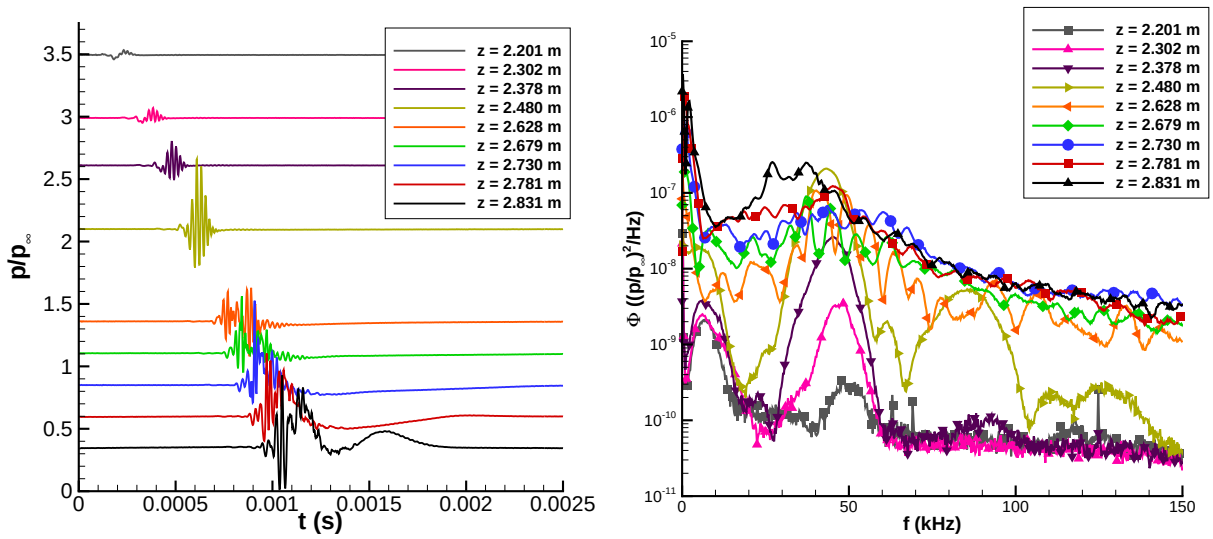


(a) (b)

**Figure 13. Ensemble-averaged disturbances from spark perturbations, $P_0$ = 1084 kPa, $T_0$ = 423.8 K, $Re = 10.8 \times 10^6/m$; (a) Pressure traces, each trace is vertically offset proportional to z; (b) Power spectral density.**

## C. Growth of Disturbances from Glow Perturbations

A glow perturber was also used to generate perturbations near the unstable frequencies measured in the naturally-occurring disturbances. These perturbations were introduced just below the maximum freestream Reynolds number for quiet flow in the BAM6QT ($Re = 10.8 \times 10^6/m$). These freestream conditions are the same as for the data shown above for the naturally-occurring spots and the highest freestream condition for the spark perturbations. Similar to the spark-perturber results, fifty samples were ensemble averaged to obtain a better representation of the data set. Figures 14 through 18 show some of the resulting ensemble-averaged pressure traces. It is immediately evident that the glow perturbations generate much smaller disturbances when compared to the spark-induced disturbances.

The largest disturbance growth from the glow perturbations was seen with an input frequency of 45 kHz (Figure 16). This frequency is smaller than seen in the natural spot development, but is in agreement with the peak frequency for the spark-perturbations. Again, this lower frequency is likely the result of the reduced fetch for wave growth caused by generating the perturbations further downstream at z = 1.924 m where the boundary layer is thicker. Even though only five cycles of the sine wave were input, the initial disturbance has grown and more cycles are visible in the disturbances as they pass by the sensors. The PSD of the signal shows that the peak frequency of the disturbance is near 47 kHz and decreases to 36 kHz as the boundary-layer thickens downstream. This peak is much narrower that seen in the spark-perturber results and is likely the result of introducing a discrete perturbation frequency instead of the broadband frequencies introduced by a spark. The amplitude of the packet increases downstream as the packet elongates. By the last few sensors, the wave packet has begun to either breakdown to turbulence or decay back to a laminar state. A small increase in broadband frequencies is seen, which could indicate the onset of transition, but more measurement length is needed to determine whether this is the case.

For other glow-perturbation input frequencies, less growth of the disturbances was seen. In these cases, by the downstream sensors, the peak amplitude decreases as the waves seem to decay back to a laminar state. It is interesting to note that for some of these disturbances, a second peak is also seen near 30 kHz. It is unclear what causes the growth of this lower frequency, as it was not seen in the natural disturbances or in the spark-perturber results. However, a similar double peak with unknown origin was also measured by Steen[22] (pg. 33) with a freestream Pitot probe under quiet flow conditions in the BAM6QT.

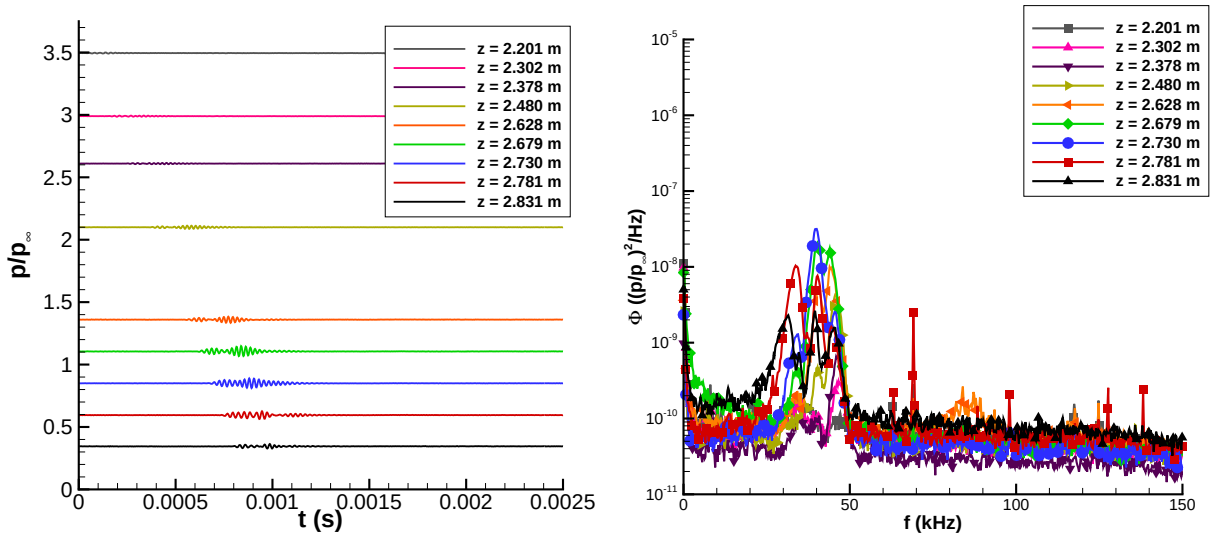


(a) (b)

**Figure 14. Ensemble-averaged disturbances from 35 kHz glow perturbations, $P_0$ = 1082 kPa, $T_0$ = 423.6 K, $Re = 10.8 \times 10^6/m$; (a) Pressure traces, each trace is vertically offset proportional to z; (b) Power spectral density.**

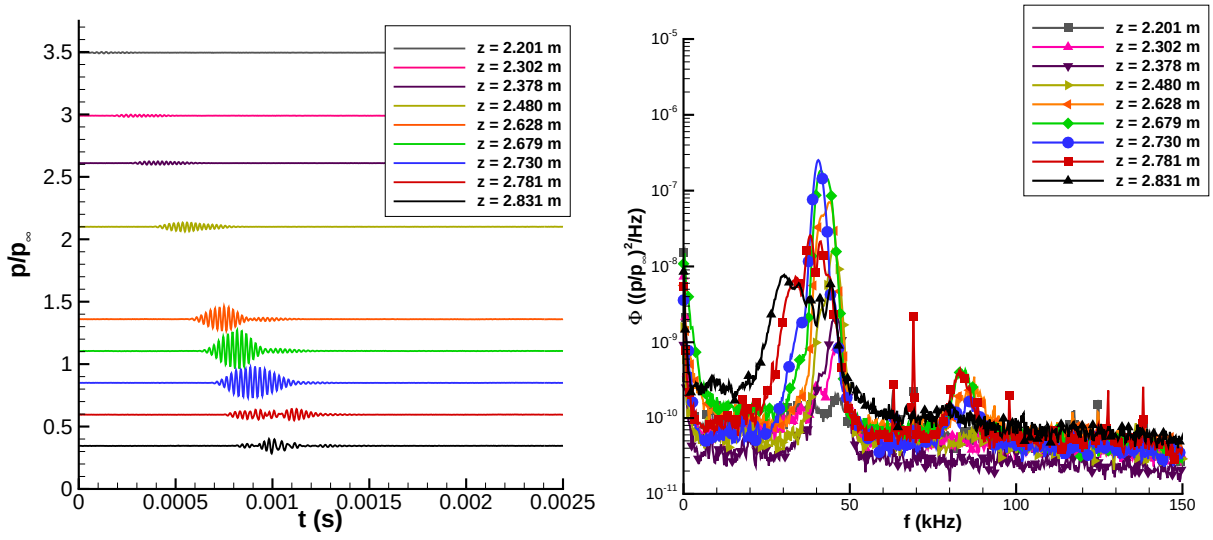


(a) (b)

**Figure 15. Ensemble-averaged disturbances from 40 kHz glow perturbations, $P_0$ = 1083 kPa, $T_0$ = 423.6 K, $Re = 10.8 \times 10^6/m$; (a) Pressure traces, each trace is vertically offset proportional to z; (b) Power spectral density.**

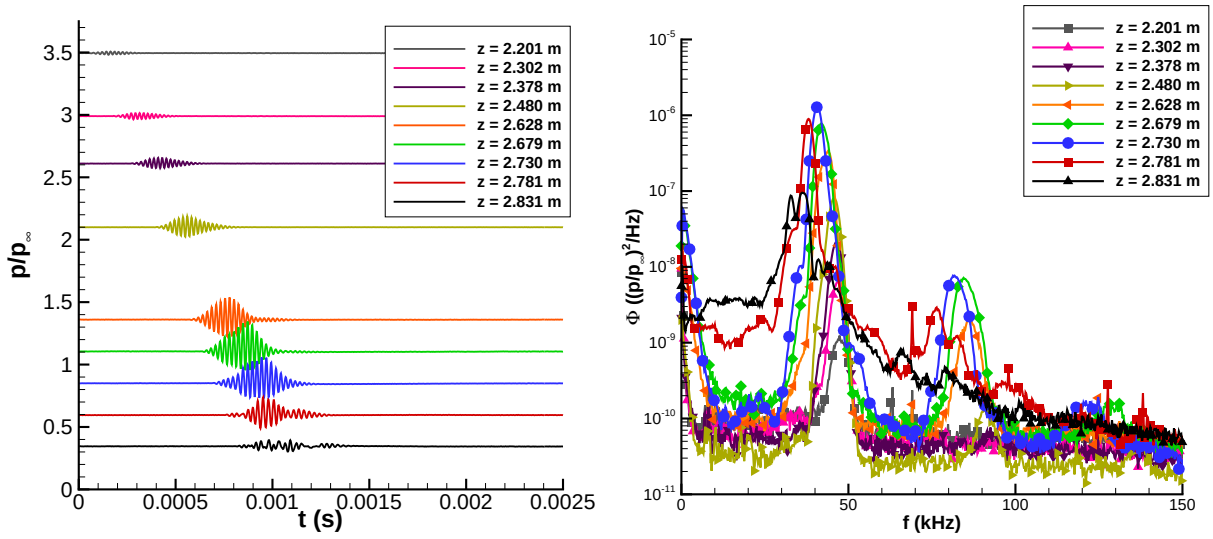


(a) (b)

**Figure 16. Ensemble-averaged disturbances from 45 kHz glow perturbations, $P_0$ = 1082 kPa, $T_0$ = 423.6 K, $Re = 10.8 \times 10^6/m$; (a) Pressure traces, each trace is vertically offset proportional to z; (b) Power spectral density.**

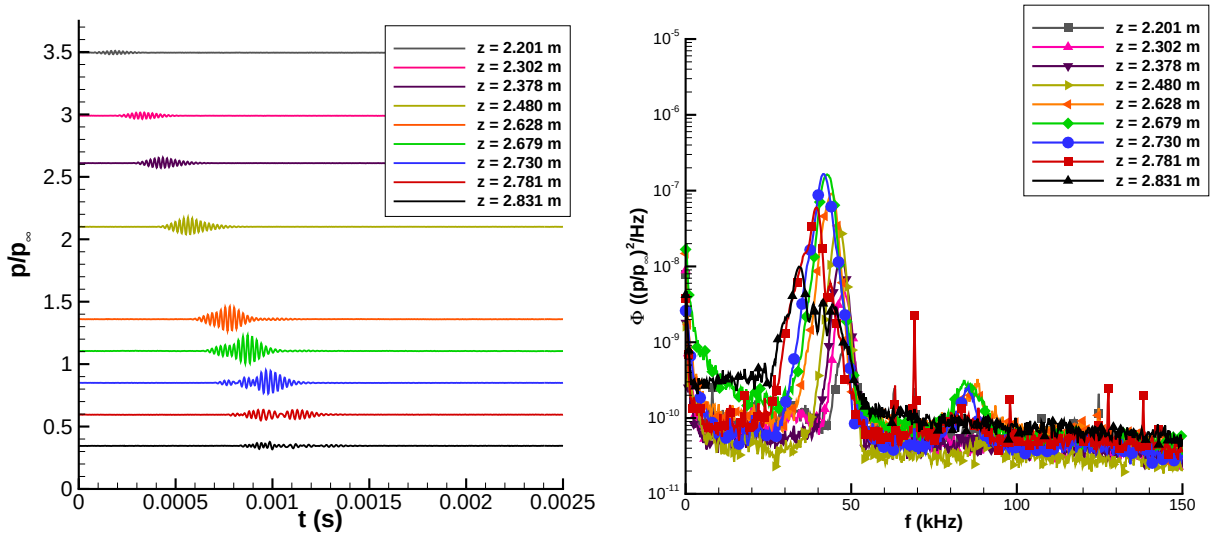


(a) (b)

**Figure 17. Ensemble-averaged disturbances from 50 kHz glow perturbations, $P_0$ = 1081 kPa, $T_0$ = 423.6 K, $Re = 10.8 \times 10^6/m$; (a) Pressure traces, each trace is vertically offset proportional to z; (b) Power spectral density.**

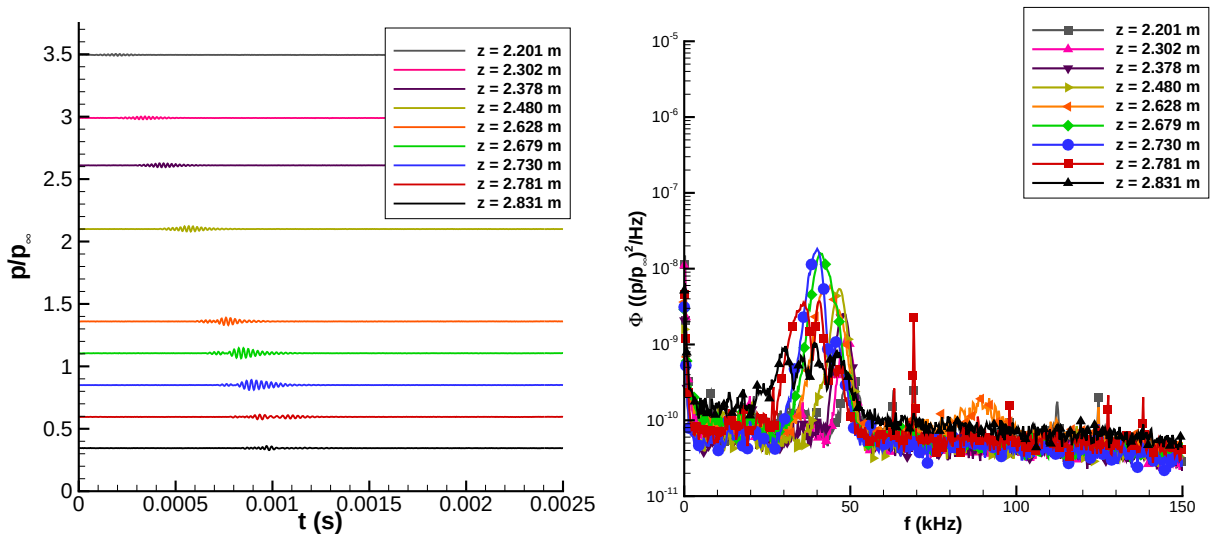


(a) (b)

**Figure 18. Ensemble-averaged disturbances from 55 kHz glow perturbations, $P_0$ = 1083 kPa, $T_0$ = 423.5 K, $Re = 10.8 \times 10^6/m$; (a) Pressure traces, each trace is offset proportional to z; (b) Power spectral density.**

## D. Repeatability of Spark and Glow Perturbations

The repeatability of the perturbations and resulting disturbances affects how well the ensemble averages repeat from run to run. To show the repeatability of the ensemble-averaged pressure traces, five repeat runs were conducted with the spark perturber at $Re = 10.8 \times 10^6/m$. Figure 19 shows similar average pressure variations from run to run, even as the wave packets break down to turbulence. Ensemble averages of smaller wave packets showed even less variation from run to run.

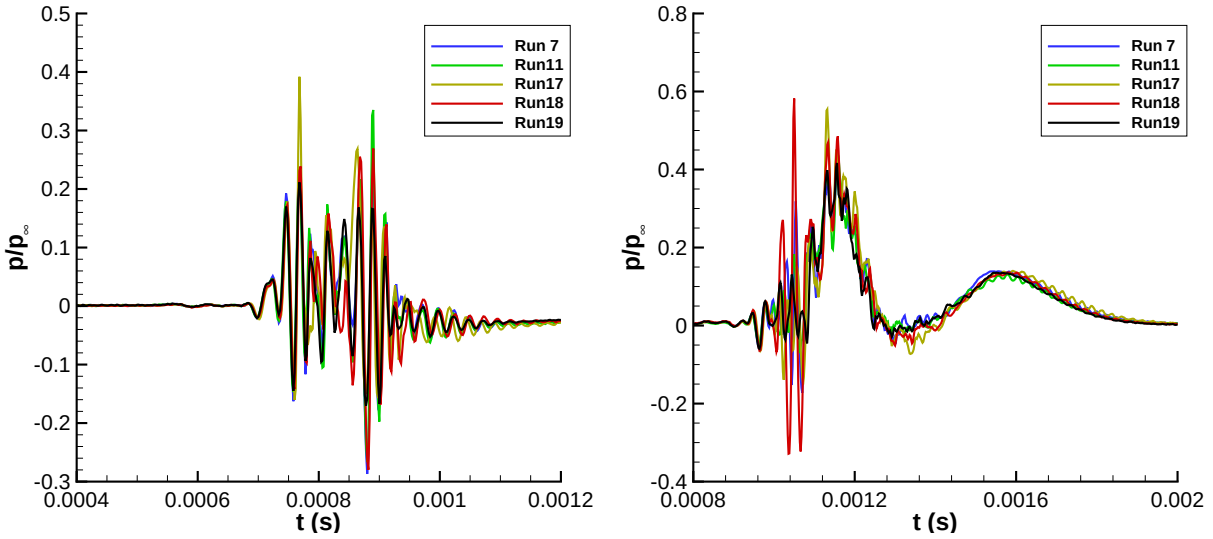


(a) (b)

**Figure 19. Repeatability of spark-perturbation ensemble averages, $P_0$ = 1084 kPa, $T_0$ = 423.8 K, $Re = 10.8 \times 10^6/m$; (a) z = 2.628 m; (b) z = 2.831 m.**

The deviation of the individual samples from the ensemble average is also important. Figure 20 shows five individual spark-perturbation samples as well as the ensemble average acquired from all fifty disturbance samples. At z = 2.302 m, the disturbance is still small and shows good repeatability. As the sample grows, variation from sample to sample increases, but there is still good repeatability. By z = 2.730 m, the packets have begun to break down. The ensemble still represents the individual samples well, but the variation between samples and the ensemble is much greater. By z = 2.831 m, the ensemble no longer represents the individual time traces. Each sample has broken down to turbulence in a different manner. As a result, the ensemble averages hide the true turbulent fluctuations present within the turbulent spots.

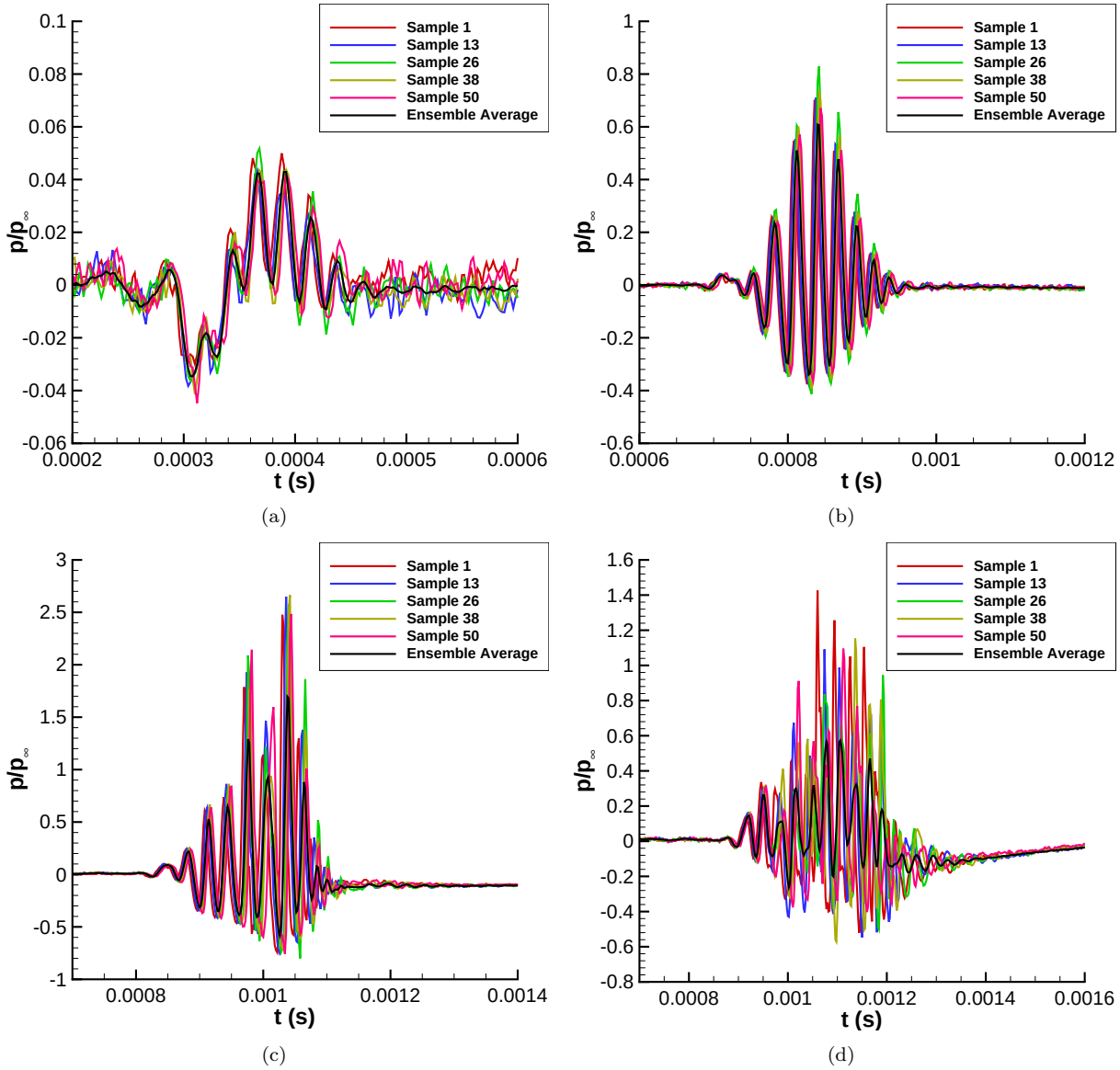


**Figure 20. Comparison of individual spark-perturbation samples to ensemble average, $P_0$ = 827.9 kPa, $T_0$ = 424.0 K, $Re = 8.25 \times 10^6/m$; (a) z = 2.302 m; (b) z = 2.628 m; (c) z = 2.730 m; (d) z = 2.831 m.**

A similar trend of increasing variation with increasing wave amplitude was seen for the glow-perturber results. However, the variation between wave packets was larger, even for wave packets that had not yet broken down. Figure 21 shows five individual glow-perturbation samples as well as the ensemble average for all fifty samples. At z = 2.302 m, the disturbance is still small and shows good repeatability. However, as the sample grows, variation from sample to sample increases much more than in the spark-perturber cases. At z = 2.730 m, the packets are large and nonlinear and show significant variation from packet to packet. This variation is primarily in magnitude and not in frequency. This larger variation may arise because of the

longer time it takes for the glow disturbance to breakdown compared to the spark. During this time, there is more opportunity for random variations to affect the disturbance growth. Despite the reduced repeatability, the ensemble-averaged results still represent the trends seen in the individual samples as they grow.

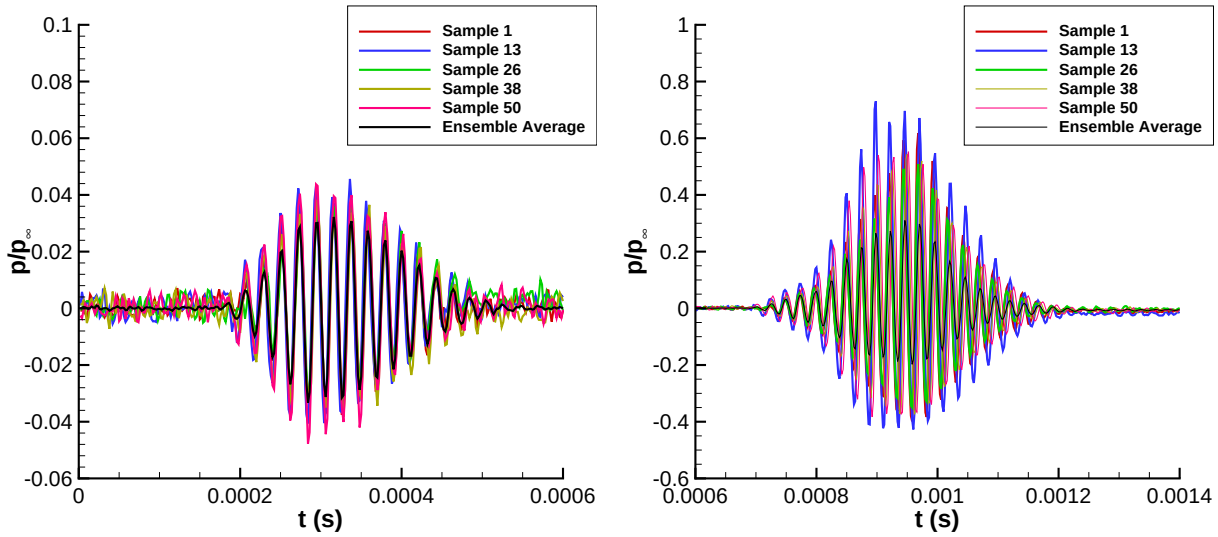


**Figure 21. Comparison of individual glow-perturbation samples to ensemble average, $P_0$ = 1082 kPa, $T_0$ = 423.6 K, $Re = 10.8 \times 10^6/m$; (a) z = 2.302 m; (b) z = 2.730 m.**

The increased sample variation from the ensemble average with wave growth is more clearly shown by looking at the standard deviation of the difference of the samples from the ensemble average. Figure 22 shows the average variation as a function of pressure fluctuation intensity. The average deviation from the ensemble average for both the spark and glow-perturbation cases increases as the disturbances grow and become nonlinear. The lower repeatability of the glow perturbations is again seen here. The standard deviation of the glow-perturber results from the ensemble average is higher than the spark-perturber results for a similar pressure fluctuation intensity.

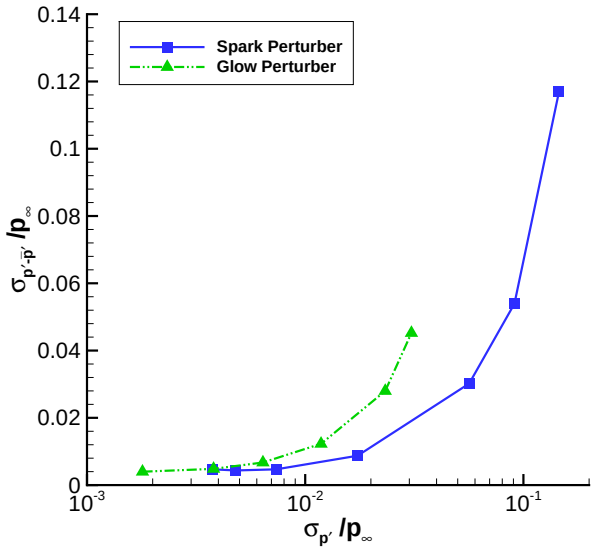


**Figure 22. Deviation of samples from ensemble average; Spark perturbations, $P_0$ = 827.9 kPa, $T_0$ = 424.0 K, $Re = 8.25 \times 10^6/m$; Glow perturbations, $P_0$ = 1082 kPa, $T_0$ = 423.6 K, $Re = 10.8 \times 10^6/m$.**

### E. Convection Velocity of Turbulent Spots

A direct determination of the convection velocity for the wave packets and turbulent spots can be made by analyzing the turbulent spot pressure traces. Figure 23 shows the leading and trailing edges of the spot marked with black lines. The convection velocities of the spots can be calculated from the slope of these lines. For the naturally-developed spot on the nozzle wall, the leading edge and trailing edge velocities are $0.93U_\infty$ and $0.67U_\infty$, respectively. However, in this case the spanwise location of the spot relative to the sensors is not known. For the spot generated by the spark perturber, the leading edge convection velocity is again $0.93U_\infty$. However, the trailing edge convection velocity is higher at $0.76U_\infty$. It should be noted that behind the spark-generated spots, there are additional second-mode fluctuations. These fluctuations occur in the lower pressure or calmed region behind the spots. Because they are out of phase, the ensemble average barely shows them. These smaller fluctuations were not included in the above estimate of the convection velocity. If these fluctuations are included, the trailing edge convection velocity is decreased to approximately $0.63\ U_\infty$.

These velocities are in general agreement with DNS computations that give a leading edge convection speed of $0.89U_\infty$ and a trailing edge convection speed of $0.68U_\infty$.[14] Joksch and Kleiser[15] also report convection velocities for wave packets at Mach-5. For an adiabatic wall, they distinguished between first mode and second mode wave propagation. The first-mode packets had leading and trailing edge convection velocities of $0.95U_\infty$ and $0.83U_\infty$, respectively. Second-mode packets had a similar $U_{le}/U_\infty$ of 0.96, but $U_{te}/U_\infty$ was only 0.54. They also plot the convection of the turbulent spots, but do not give computed values.

Experimental measurements give similar results. Previous high-speed experiments used heat transfer measurements to detect and track the turbulent spots under different flow conditions.[18,28,29] In each case, the spots occurred naturally, and therefore, the spanwise location of the spot relative to the sensor is unknown. This results in a lot of scatter in the computed velocities. These high-speed results give a range of $U_{le}/U_\infty$ from 0.81–0.94. The trailing edge convection velocity varies from 0.41–0.63. Zanchetta (pg. 195) also presents a summary of convection velocities from selected experiments at lower speeds for both natural and artificially generated turbulent spots. These lower speed values ranged from $U_{le}/U_\infty = 0.8 - 0.93$ and $U_{te}/U_\infty = 0.5 - 0.69$. The effect of any pressure gradient[30,31] on these results has not been considered here.

The present result for the leading edge convection velocity lies at the upper end of the existing data. The present estimate of $U_{te}/U_\infty$ =0.76 is higher than the existing range of results. However, if the lower trailing edge convection velocity of 0.63 $U_\infty$ is considered, it lies at the upper range of existing values.

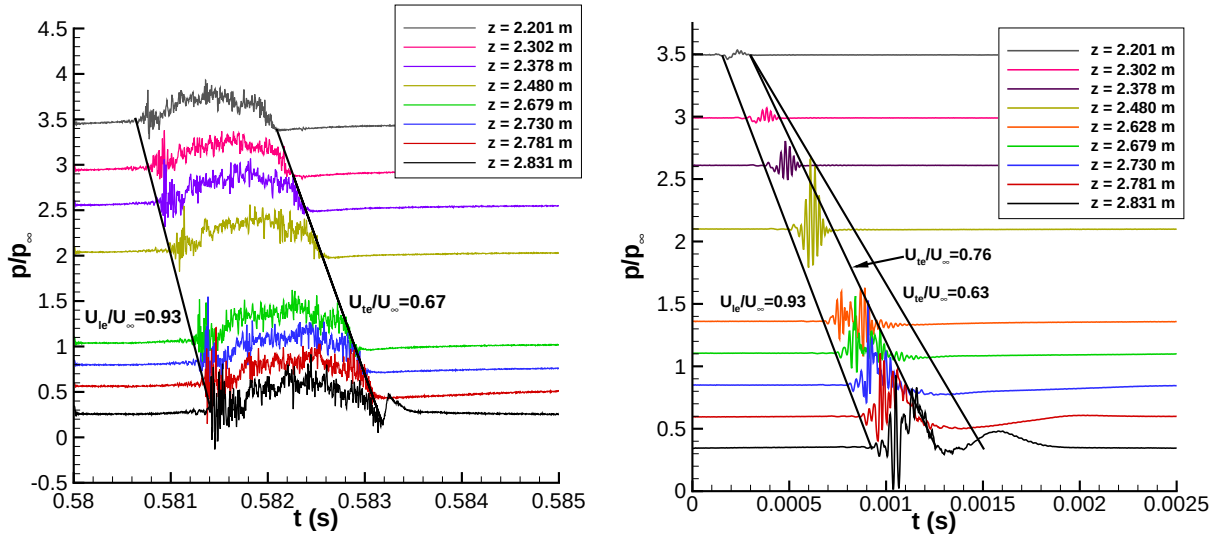


**Figure 23. Convection velocities; (a) Large, naturally occurring turbulent spot, $P_0$ = 1142 kPa, $T_0$ = 428.3 K, $Re = 11.2 \times 10^6/m$; (b) Spark-generated spot, $P_0$ = 1084 kPa, $T_0$ = 423.8 K, $Re = 10.8 \times 10^6/m$.**

### F. Amplitudes Near Breakdown

Finding an amplitude criteria at which perturbations become nonlinear and breakdown is important for predicting boundary layer transition. In order to study the amplitude of the measured disturbances, the pressure fluctuation intensity, $\sigma_{p'}/p_\infty$, was plotted for varying $Re$ (Figure 24(a)). The fluctuation intensity was computed by integrating under the ensemble-averaged PSD and taking the square root.

At $Re = 5.8 \times 10^6/m$, the fluctuation intensity grows slowly. Nonlinearity of the waves is first indicated by the presence of a very small harmonic rising above the above the noise level in the PSD at z = 2.730 m (Figure 9(b)). The wave continues to grow nonlinearly downstream and no evidence of breakdown is seen. Between $Re = 6.3 - 7.6 \times 10^6/m$, the wave grows nonlinearly further upstream, as indicated by the growth of harmonics in the PSD. By the last few sensors, the $\sigma_{p'}/p_\infty$ begins to decrease, indicating wave breakdown. These results are in agreement with the PSD's that show the second-mode peak decreasing in amplitude as the broadband frequencies increase. The next case at $Re = 8.3 \times 10^6/m$ captures the largest fluctuation intensity of 20% of $p_\infty$ before the waves break down. Looking at the power spectra at this location, the peak frequency is only slightly smaller than at the previous sensor location (Figure 11(b)). The spectra also shows many nonlinear peaks among large broadband frequencies. By the next sensor location, the peaks have decreased further in amplitude, below the broadband frequencies.

The remaining higher freestream conditions do not seem to capture the peak fluctuations at breakdown because of the long space with no instrumentation between the last nozzle sensor and the first pipe insert sensor. For $Re = 8.9 \times 10^6/m$, breakdown occurs between z = 2.628 and 2.679 m. For the highest cases, breakdown occurs somewhere between z = 2.480 and 2.628 m. Therefore, the best cases to define an amplitude criteria for wave breakdown are at $Re = 7.6$ and $8.3 \times 10^6/m$ when the pressure fluctuation intensity is 15–20% of the freestream pressure. It is unclear whether this amplitude criteria applies at the other freestream conditions when breakdown occurs earlier on the nozzle wall.

The best conditions to define an amplitude criteria for nonlinearity are at the highest $Re$ where the signal to noise ratio is the best. Wave amplitudes near 1.5–1.8% of the freestream pressure clearly show the presence of harmonics in the PSD's, indicating nonlinearity. However, it should be noted that this amplitude could even be smaller if the nonlinearity in the measurements is masked by the background electronic noise. Indeed, when the harmonics first appear in the PSD, their signal to noise ratio is small.

A different pattern for wave growth is seen in the glow-perturbation results (Figure 24(b)). In all cases, the amplitude of the waves is smaller than the corresponding spark-perturber case. As shown before, growth of the glow-induced disturbances is highly dependent on the input disturbance frequency. An input frequency of 45 kHz shows the highest growth, while other frequencies show much lower growth before they decay back to a laminar state. The 45 kHz perturbation does grow to an RMS of 6%, but it is unclear whether transition is beginning by the last sensors or if the disturbance is decaying back to a laminar state. However, these results show a an amplitude near 1–1.5% for nonlinearity of the wave packets, again indicated by the presence of the harmonics in the PSD's.

## V. Concluding Remarks

The pressure fluctuations beneath turbulent spots and wave packets were measured on the nozzle wall of the BAM6QT. These seem to be the first experimental measurements of pressure fluctuations associated with turbulent spots in a hypersonic boundary layer. Previous experimental measurements have primarily used thin-film heat-transfer gages to study hypersonic turbulent spots.[18,28,29,32] In contrast to the very thin boundary layer found on most wind-tunnel models, the thick laminar boundary layer on the nozzle wall of the BAM6QT allowed the study of the turbulent spots with pressure transducers at resolvable frequencies.

Natural disturbances that break down into turbulent spots were studied for the nozzle wall with no external perturbation. Two types of natural disturbances were found: large turbulent spots that develop near the throat and fill almost the entire nozzle circumference and smaller wave packets that breakdown into smaller turbulent spot downstream in the nozzle. These wave packets have frequencies near 60 kHz at $Re = 10.6 \times 10^6/m$. Those frequencies agree with computations of second-mode waves on the nozzle wall, showing that second-mode waves seem to dominate transition far downstream in the BAM6QT. Measurements of the natural disturbances also showed laminar flow was maintained at least 0.254 m downstream of the nozzle exit, indicating that the quiet-flow test core in the tunnel extends downstream of the test section.

The natural disturbances were compared to controlled disturbances created by glow and spark perturbations. Detailed centerline measurements were made behind these artificially-generated turbulent spots.

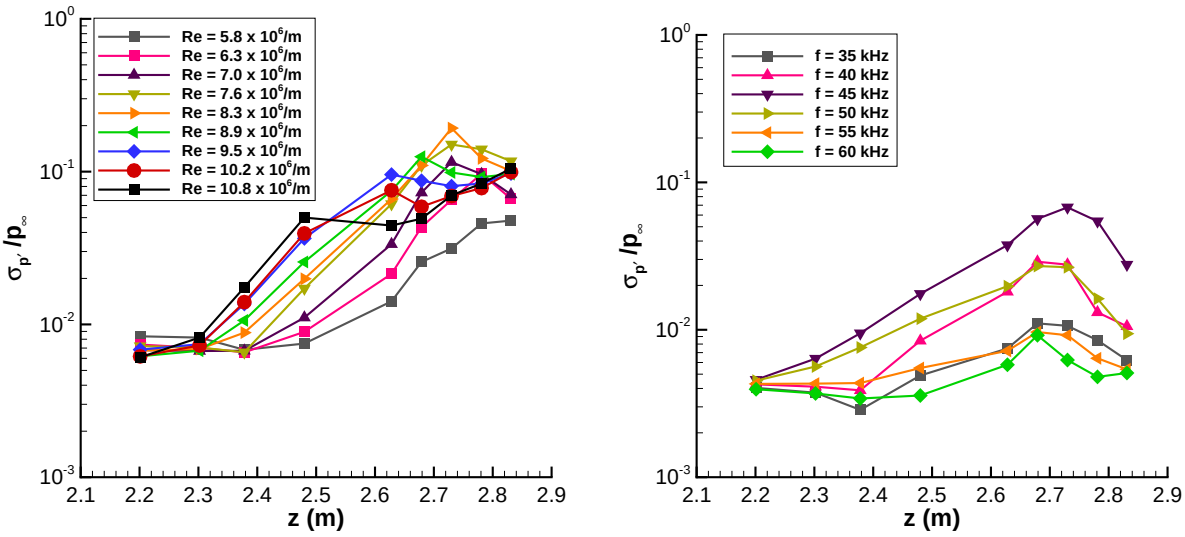


(a) (b)

**Figure 24. Variation of pressure-fluctuation intensity with downstream distance; (a) Spark-generated disturbances; (b) Glow-generated disturbances at** $Re = 10.8 \times 10^6/m$**.**

Spark perturbations created large disturbances that broke down into turbulent spots. The peak frequency of the disturbances was near 45 kHz at $Re = 10.8 \times 10^6/m$. This frequency is smaller than the second-mode frequencies measured in the natural disturbances, presumably due to the reduced fetch and thicker boundary layer where the perturbations are introduced. The spark-perturber results clearly showed the complete process of wave growth and breakdown into a turbulent spot. Nonlinear wave growth began at a pressure fluctuation intensity near 1.5–1.8% of the freestream pressure. Breakdown of the wave did not occur until near 15–20% of the freestream pressure.

The glow perturbations created much smaller disturbances than the spark perturbations. Input frequencies near 45 kHz created disturbances that grew the most at $Re = 10.8 \times 10^6/m$, in agreement with the spark-perturber results. The wave packets showed nonlinearity at a slightly smaller amplitude than spark-perturber results (near 1-1.5% of the freestream pressure). However, it is unclear whether the glow-perturber results were breaking down into turbulence or decaying back to a laminar state. Other input frequencies were less effective and showed less wave growth.

Current measurements have explored the centerline of artificially generated turbulent spots and obtained pressure fluctuations along the centerline as well as convection velocities of the turbulent spots. The growth and breakdown of instability waves into turbulent spots has been shown to be a continual process where both second-mode waves and turbulent fluctuations are simultaneously observed over a long region. Future measurements will place sensors off centerline to study the spanwise features of the turbulent spots. This information along with the data presented here can be used to more accurately model transitional pressure fluctuations when using a turbulent-spot based model of transition.

## Acknowledgments

This work could not have been completed without the help of John Phillips, the Purdue AAE department electronics technician, who designed and built the spark perturber used for these measurements. Peter Gilbert provided the CAD model used to generate Figure 3. Funding was provided in part by a National Defense Science and Engineering Graduate Fellowship, the National Science Foundation Graduate Research Fellowship Program, Sandia National Laboratories, and AFOSR.

# References


[1]Houbolt, J. C., "On the Estimation of Pressure Fluctuations in Boundary Layers and Wakes," GE TIS66SD296, April 1966.

[2]Lowson, M. V., "Prediction of Boundary Layer Pressure Fluctuations," AFFDL-TR-67-167, April 1968, Citation AD0832715 in DTIC.

[3]Martellucci, A., Chaump, L., Rogers, D., and Smith, D., "Experimental Determination of the Aeroacoustic Environment about a Slender Cone," *AIAA Journal*, Vol. 11, No. 5, 1973, pp. 635–642.

[4]Chaump, L. E., Martellucci, A., and Monfort, A., "Aeroacoustic Loads Associated with High Beta Re-entry Vehicles," AFFDL-TR-72-138, May 1973, Volume I.

[5]Raman, K. R., "Surface Pressure Fluctuations in Hypersonic Turbulent Boundary Layers," AIAA Paper 73-997, October 1973.

[6]Laganelli, A. L., Martellucci, A., and Shaw, L. L., "Wall Pressure Fluctuations in Attached Boundary-Layer Flow," *AIAA Journal*, Vol. 21, No. 4, 1983, pp. 495–502.

[7]Pate, S. R. and Brown, M. D., "Acoustic Measurements in Supersonic Transitional Boundary Layers," AEDC-TR-69-182, October 1969.

[8]Johnson, R. I., Macourek, M. N., and Saunders, H., "Boundary Layer Acoustic Measurements in Transitional and Turbulent Flow at $M_\infty = 4.0$," AIAA Paper 69-344, April 1969.

[9]Cassanto, J. M. and Rogers, D. A., "An Experiment to Determine Nose Tip Transition with Fluctuating Pressure Measurements," *AIAA Journal*, Vol. 13, No. 10, October 1975, pp. 1257–1258.

[10]Pate, S. R., "Dominance of Radiated Aerodynamic Noise on Boundary-Layer Transition in Supersonic/Hypersonic Wind Tunnels," AEDC-TR-77-107, March 1978.

[11]Jones, T. V. and Lagraff, J. E., "Turbulent Spot Growth Rates and Generation in a Compressible Boundary Layer," AFOSR-TR-96-0070, October 1995, Citation ADA304396 in DTIC.

[12]Vinod, N. and Govindarajan, R., "Pattern of Breakdown of Laminar Flow into Turbulent Spots," *Physical Review Letters*, Vol. 93, No. 11, September 2004.

[13]Zharov, V. A., Htun, H., and Khlopkov, Y. I., "Statistical Modeling of the Turbulent Transition in the Boundary Layer," *Journal of Applied Mechanics and Technical Physics*, Vol. 50, No. 5, 2009, pp. 742–746.

[14]Krishnan, L. and Sandham, N. D., "Effect of Mach Number on the Structure of Turbulent Spots," *Journal of Fluid Mechanics*, Vol. 566, 2006, pp. 225–234.

[15]Joksch, A. and Kleiser, L., "Growth of Turbulent Spots in High-Speed Boundary Layers on a Flat Plate," *International Journal of Heat and Fluid Flow*, Vol. 29, 2008, pp. 1543–1557.

[16]Sivasubramanian, J. and Fasel, H. F., "Direct Numerical Simulation of a Turbulent Spot in a Cone Boundary-Layer at Mach 6," AIAA Paper 2010-4599, June 2010.

[17]Casper, K. M., *Hypersonic Wind-Tunnel Measurements of Boundary-Layer Pressure Fluctuations*, Master's thesis, Purdue University School of Aeronautics & Astronautics, August 2009.

[18]Zanchetta, M., *Kinetic Heating and Transition Studies at Hypersonic Speeds*, Ph.D. thesis, Imperial College of Science, Technology, and Medicine, April 1996.

[19]Patil, M. S., Mathew, J., and RejendraKumar, P. K., "Bearing Signature Analysis as a Medium for Fault Detection: A Review," *Journal of Tribology*, Vol. 130, January 2008.

[20]Keyes, F. G., "A Summary of Viscosity and Heat-Conduction Data for He, A, $H_2, O_2$, CO, $CO_2, H_2O$, and Air," *Transactions of the ASME*, Vol. 73, 1951, pp. 589–596.

[21]Juliano, T., Segura, R., Borg, M., Casper, K., Hannon, M., Wheaton, B., and Schneider, S., "Starting Issues and Forward-Facing Cavity Resonance in a Hypersonic Quiet Tunnel," AIAA Paper 2008-3730, June 2008.

[22]Steen, L. E., *Characterization and Development of Nozzles for a Hypersonic Quiet Wind Tunnel*, Master's thesis, Purdue University School of Aeronautics & Astronautics, December 2010.

[23]Schneider, S. P., "The Development of Hypersonic Quiet Tunnels," *Journal of Spacecraft and Rockets*, Vol. 45, No. 4, 2008, pp. 641–664.

[24]Ladoon, D. W., *Wave Packets Generated by a Surface Glow Discharge on a Cone at Mach 4*, Ph.D. thesis, Purdue University School of Aeronautics & Astronautics, December 1998.

[25]Borg, M. P., *Characteristics of the Contraction of the Boeing/AFOSR Mach-6 Quiet Tunnel*, Master's thesis, Purdue University School of Aeronautics & Astronautics, December 2005, Available from DTIC as ADA441151.

[26]Schneider, S. P., "Design of a Mach-6 Quiet-Flow Wind-Tunnel Nozzle using the e**N Method for Transition Estimation," AIAA Paper 98-0547, January 1998.

[27]Glezer, A., Katz, Y., and Wygnanski, I., "On the Breakdown of the Wave Packet Trailing a Turbulent Spot in a Laminar Boundary Layer," *Journal of Fluid Mechanics*, Vol. 198, 1989, pp. 1–26.

[28]Mee, D. J., "Boundary-Layer Transition Measurements in Hypervelocity Flows in a Shock Tunnel," *AIAA Journal*, Vol. 40, No. 8, 2002, pp. 1542–1548.

[29]Fiala, A., Hillier, R., Mallinson, S. G., and Wijesinghe, H. S., "Heat Transfer Measurement of Turbulent Spots in a Hypersonic Blunt-Body Boundary Layer," *Journal of Fluid Mechanics*, Vol. 555, 2006, pp. 81–111.

[30]Katz, Y., Seifert, A., and Wygnanski, I., "On the Evolution of the Turbulent Spot in a Laminar Boundary Layer with a Favourable Pressure Gradient," *Journal of Fluid Mechanics*, Vol. 221, 1990, pp. 1–22.

[31]Seifert, A. and Wygnanski, I., "On Turbulent Spots in a Laminar Boundary Layer Subjected to a Self-Similar Adverse Pressure Gradient," *Journal of Fluid Mechanics*, Vol. 296, 1995, pp. 185–209.

[32]Wadhams, T., Mundy, E., MacLean, M. G., and Holden, M. S., "Ground Test Studies of the HIFIRE-1 Transition Experiment Part 1:Experimental Results," *Journal of Spacecraft and Rockets*, Vol. 45, No. 6, November-December 2008, pp. 1134–1148.